The performance of 2D array detectors for light sheet based fluorescence correlation spectroscopy

Anand Pratap Singh,[1,4] Jan Wolfgang Krieger,[2,4] Jan Buchholz,[2] Edoardo Charbon,[3] Jörg Langowski,[2] and Thorsten Wohland[1,*]

[1] *Departments of Biological Sciences and Chemistry and NUS Centre for Bio-Imaging Sciences, National University of Singapore, 14 Science Drive 4 ,117557, Singapore*
[2] *German Cancer Research Centre (DKFZ), Biophysics of Macromolecules, Im Neuenheimer Feld 580, D-69120 Heidelberg, Germany*
[3] *Technische Universiteit Delft, Mekelweg 4, 2628 CD Delft, The Netherlands*

[4] *Anand Pratap Singh and Jan Wolfgang Krieger contributed equally to this work.*

[*]*dbswt@nus.edu.sg*

References and links

1. K. Greger, J. Swoger, and E. H. K. Stelzer, "Basic building units and properties of a fluorescence single plane illumination microscope," Rev. Sci. Instrum. **78**, 023705 (2007).
2. L. Carrara, C. Niclass, N. Scheidegger, H. Shea, and E. Charbon, "A gamma, x-ray and high energy proton radiation-tolerant CIS for space applications" in "IEEE International Solid-State Circuits Conference," (IEEE, 2009), pp. 40–41.
3. C. Niclass, Favi, Claudio, T. Kluter, M. Gersbach, and E. Charbon, "A 128x128 Single-Photon Imager with on-Chip Column-Level 97ps 10bit Time-to-Digital-Converter Array" in "IEEE International Solid-State Circuits Conference," (IEEE, 2008), pp 3–5.
4. J. Buchholz, J. W. Krieger, G. Mocsár, B. Kreith, E. Charbon, G. Vámosi, U. Kebschull, and J. Langöwski, "FPGA implementation of a 32x32 autocorrelator array for analysis of fast image series," Opt. Express **20**, 17767 (2012).
5. J. W. Krieger and J. Langöwski, "Quickfit 3.0: A data evaluation application for biophysics," http://www.dkfz.de/Macromol/quickfit/ (2013).
6. X. Pan, W. Foo, W. Lim, M. H. Y. Fok, P. Liu, H. Yu, I. Maruyama, and T. Wohland, "Multifunctional fluorescence correlation microscope for intracellular and microfluidic measurements," Rev. Sci. Instrum. **78**, 053711 (2007).
7. P. Kapusta, "Absolute diffusion coefficients: compilation of reference data for FCS calibration," Pico-Quant pp. 0–1 (2010).
8. M. Wachsmuth, "Fluoreszenzfluktuationsmikroskopie: Entwicklung eines Prototyps, Theorie und Messung der Beweglichkeit von Biomolekülen im Zellkern: Doctoral dissetation," Ruprecht-Karls-Universität ,Heidelberg. (2001).
9. M. Brinkmeier, K. Dörre, J. Stephan, and M. Eigen, "Two-beam cross-correlation: a method to characterize transport phenomena in micrometer-sized structures," Anal. Chem. **71**, 609–616 (2009).
10. N. Bag, J. Sankaran, A. Paul, R. S. Kraut, and T. Wohland, "Calibration and limits of camera-based fluorescence correlation spectroscopy: a supported lipid bilayer study," ChemPhysChem. **13**, 2784–94 (2012).
11. T. Wocjan, J.W. Krieger, O. Krichevsky and J. Langowski, "Dynamics of a fluorophore attached to superhelical DNA: FCS experiments simulated by Brownian dynamics," ChemPhysChem. **11**, 10671–10681 (2009).
12. B. E. Saleh and M. C. Teich, *Fundamentals of Photonics* (Wiley, 1991), pp. 83.
13. M. Brinkmeier, K. D̈orre, J. Stephan and M. Eigen, "Two-Beam Cross-Correlation: A Method To Characterize Transport Phenomena in Micrometer-Sized Structures, " Anal. Chem. **71**, 10671–10681 (1999).

S1. Description of the Microscopes

We used several microscopes to acquire the data presented in the main text: Two SPIMs and two confocal microscopes where one is situated in Singapore (no. -1) and one in Heidelberg

(no. -2) each. In this article we only gave a short summary of the setups, here we give a detailed description.

S1.1. SPIM-1

We used a custom built selective plane illumination microscope (SPIM) described in [1] (shown in Fig. S1). A laser (491+532 Dual Calypso, DPSS laser, Photonitech Pte Ltd, Singapore) passes through a laser cleanup filter (LL01-491-25, Semrock Inc., New York) to select the 491 nm laser beam and the laser beam is expanded 4 times by a set of achromatic lenses ($f_1 = 25$ mm and $f_2 = 100$ mm, Edmund optics, Singapore). It then passes through an achromatic cylindrical lens ($f = 75$ mm, Edmund optics, Singapore), which was mounted on a combination of linear and rotation stages (z-stage: MVT 40B-Z, rotation stage: DT 40-D25, all stages from OWIS, Staufen, Germany). The resulting beam over-illuminates the back focal aperture of the low NA illumination objective (SLMPlan 20X /0.25, Olympus, Singapore) to obtain a $\sim 1.4\ \mu$m thin light sheet. The illumination objective has a working distance of WD = 21 mm. This provides the necessary space to bring the light sheet into the focal plane of the detection objective (LUMPLFLN 60x/1.0 W, WD = 2.0 mm, Olympus, Singapore). The sample mounting unit consists of a custom built sample chamber (Physics mechanical workshop, NUS, Singapore) and motorized linear x-, y- and z-stages together with a rotation stage (XYZ-linear stages: $3\times$ 8MT184-13DC and rotation stage: 8MR174-1-20, Standa Ltd., Vilnius, Lithuania). The detection objective is mounted on a piezo flexure objective scanner (P-721 PIFOC, Physik Instruments, Singapore) to control the objective in nm precision. Fluorescence emission filters (FF02-534/30-25, Semrock Inc., New York) were mounted behind the detection objective in a computer controlled motorized filter wheel (6 slotted, OWIS, Staufen, Germany). A standard tube lens (part no. LU074700, $f = 180$ mm, Olympus, Singapore) is used to image the sample onto a camera. We mounted one of several available models: Andor *iXon X3 860* EMCCD camera (Andor Technology, Belfast, UK), *Evolve 512* EMCCD camera (Photometrics, Tucson, United States), *ORCA-Flash4.0* sCMOS Camera (Hamamatsu, Hamamatsu city, Japan) or a
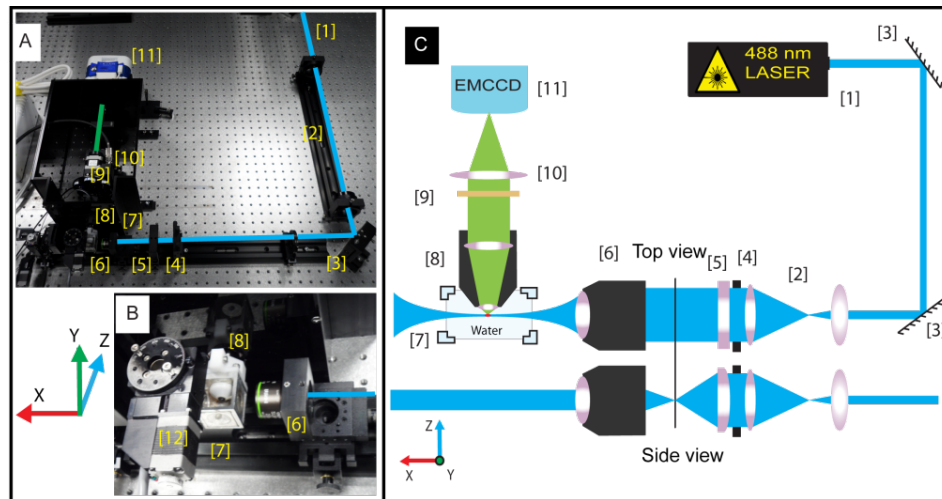

Fig. S1. Schematic view of SPIM-1: [1] laser, [2] 3-4x beam expansion, [3] mirror, [4] *xy*-slit, [5] cylindrical lens, [6] illumination objective 20x/NA0.25, [7] sample chamber, [8] detection objective 60x/NA1.0 W, [9] filter wheel, [10] tube lens, [11] camera, [12] translation and rotation stages (XYZR stages)

SA-05 CMOS camera (Dynamic Analysis System Pte Ltd., Singapore).

The SPIM-flow measurements were perfomed by mounting the microchannel vertically into the microscope without using the sample chamber, see Fig. S2. The fluorescence was collected using a 10x / NA 0.3 air objective (UPlanFL N, Olympus, Singapore) for detection, instead of the usual 60x objective.
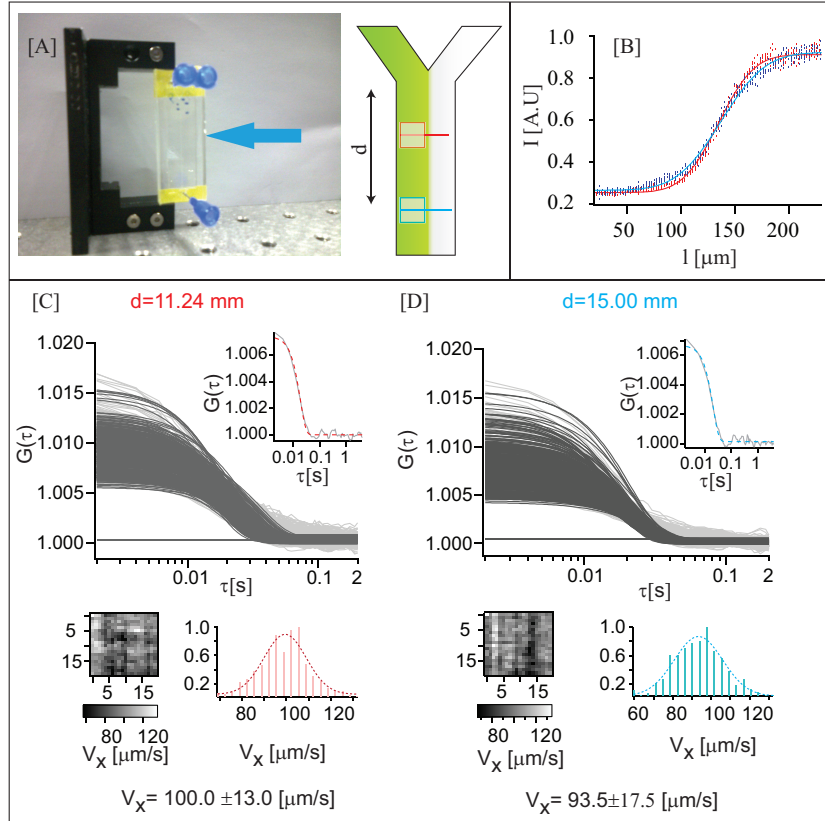

Fig. S2. Microchannel flow measurement in SPIM: [A] a photograph and sketch of the Y-shaped microchannel, [B] intensity profile across the microchannel at the two positions marked red and blue in [A]. The lines represent fits as described in the article; [C] SPIM-FCS autocorrelation functions (top) and velocity fit result images and histograms (bottom) from fits to this measurement.

S1.2. SPIM-2

The SPAD array measurements were performed on a second custom SPIM setup with comparable characteristics and also based on the design described in [1]. For a photograph see Fig. S3 and for a sketch of the beam path Fig. S4. A 491 nm DPSS laser (Calypso, Cobolt AB, Solna, Sweden) is expanded 5-fold (1x-8x zoom beam expander S6ASS2075/067, Sill Optics GmbH & Co KG, Wendelstein, Germany) and then relayed and further magnified 3x with a pair of lenses (AC508-100-A-ML + AC508-300-A-ML, Thorlabs GmbH, Dachau, Germany) onto a cylindrical lens with focal length $f = 100$ mm (CKX18-C, Newport Spectra-Physics GmbH, Darmstadt) and finally a projection objective (Nikon Plan Fluor 10x/NA0.3). The samples are mounted inside a water-filled sample-chamber from stainless steel and may be moved using motorized XYZ-stages (3× M-112.2DG with 3× C-863 Mercury controller,

Physik Instrumente, Karlsruhe, Germany). Detection is done using a Nikon CFI Apo-W NIR 60x/NA1.0 water dipping objective. The light is then filtered by a 500 nm long-pass filter (Edge Basic 488LP, Semrock, Rochester, USA), which suppresses scattered light by about a factor of 10^6 at 491 nm. The fluorescence light is then split with a 50:50 beam splitter plate and either imaged onto an Andor *iXon X3 860* EMCCD-camera (Andor, Belfast), using a Nikon tube lens ($f = 200$ mm, MXA20696, Nikon GmbH, Düsseldorf, Germany), or onto the SPAD array *Radhard2* [2] by a $f = 100$ mm achromatic lens (AC254-100-A-ML, Thorlabs GmbH, Dachau, Germany). This results in a 60x magnification for the EMCCD-camera (pixel-size 24×24 μm^2, i.e. $400 \times 400n$ nm^2 in the object plane) and a 30x magnification for the SPAD array (pixel-pitch: 30 μm, i.e. 1000 nm in the object plane and SPAD diameter: 4 μm, i.e. 133.3 nm in the object plane). The lower magnification (note, not a lower NA) for the SPAD array was chosen to increase the intensity measured on each SPAD 4-fold compared to a 2-fold loss in magnification/pixel-separation.

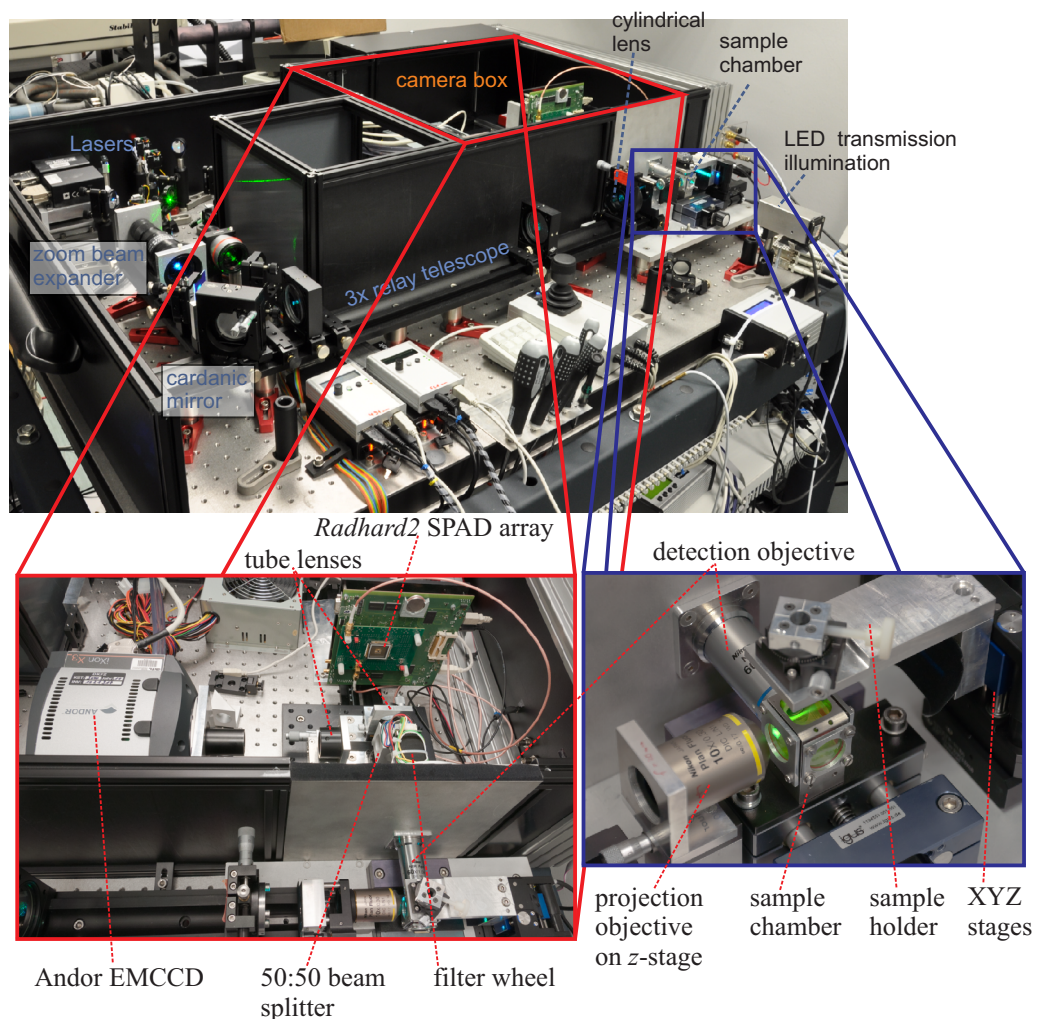The SPAD array is made up of 32×32 single-photon avalanche diodes (SPAD) with an
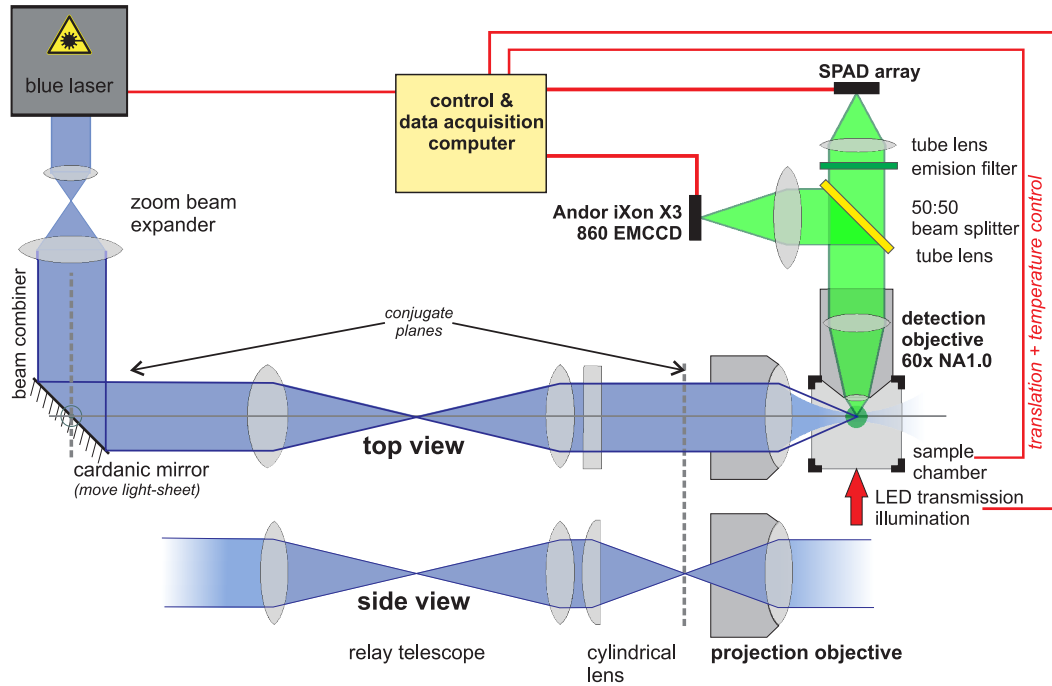

Fig. S3. Photograph of SPIM-2

Fig. S4. Schematic sketch of SPIM-2

active area diameter of 4 μm and a spacing of 30 μm (see Fig. S5). This results in a fill factor of around 1.4%. The remaining space is used for passive quenching electronics, a 1-bit memory and readout electronics. Hence, each frame contains information on whether at least one photon has been detected in each SPAD or not. The quantum efficiency of the SPAD is 35% @ 525nm with a dark-count rate (DCR) of about 155Hz (at room temperature). The SPADs were operated at an excess voltage level of 2 V above their break-down voltage. The sensor is mounted on a LASP development board [3], containing two Virtex-II Pro (XC2VP40, Xilinx, San Jose, USA) field programmable gate arrays (FPGA) for data readout and image processing. We use a modified processing mode as described in our earlier publication [4]:
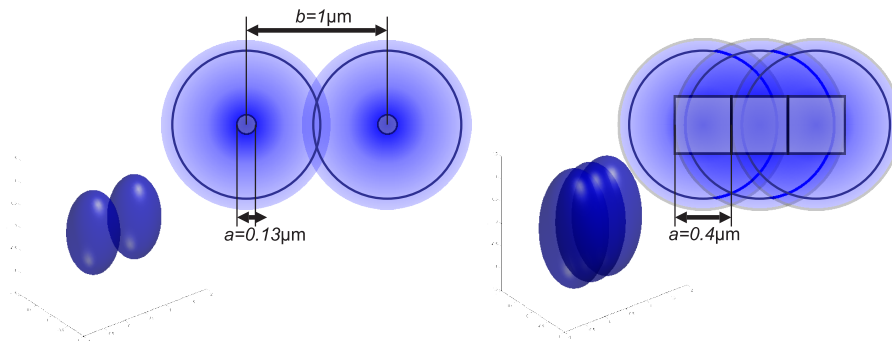

Fig. S5. Schematic view of the observation foci (assumes to be Gaussian) for the *Radhard2* sensor (left) and an *iXon X3 860* EMCCD camera (right).

The implemented FPGA design can read the sensor in 2.66 μs frame time for full frames and down to 300 ns for a region of interest (ROI) of 4 lines. We calculate the autocorrelation functions for each of the 1024 SPADs in real time at a minimum lag time of $\tau_{min} = 10$ μs. To account for the mismatch in time scales between readout and minimal lag time, we added an optional 2-bit counter (situated in the FPGA) for each SPAD, summing up three consecutive frames before sending them to the correlators. This helps solving some of the clipping problems already mentioned in [4] Buchholz et al. The computed correlation function, and if the bandwidth allows it, the raw data are then sent via two USB 2.0 connections to a Linux-PC, which controls the whole SPIM setup and both image sensors using our custom control and data evaluation software QuickFit 3.0 [5].

S1.3. Sample-bags for SPIM-FCS

The bead solutions (typically $20 - 50$ μl) were mounted in transparent (UV-VIS-IR transparency: 90%), heat sealed plastic bags (fluorinated ethylene propylene films, thickness 13.0 μm, refractive index $1.341 - 1.347$, Katco Ltd., United Kingdom, or Lumox Folie 25 M, thickness 25 μm, Sarstedt AG & Co, Nümbrecht, Germany). Fig. S6 shows a photograph of these sample bags, filled with a bead solution. The sample bags were created by cutting a rectangular patch of foil which is folded once and sealed into a tube. Then one end is closed, the sample is filled in and the other end is closed. We cleaned the foil with 70% ethanol and distilled water to remove any dirt. The bags were sealed using either a custom built temperature-controlled soldering tweazer (Tweezer ZD-409, voltage: 230V, heating power: 48W, reichelt elektronik GmbH & Co. KG, Sande, Germany) or a plastic bag sealer (kingstar impulse sealer, Kingstar Packing Machine ltd.
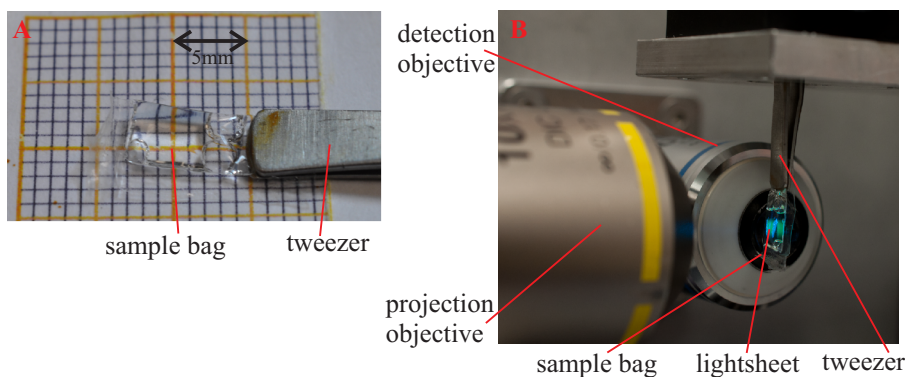

Fig. S6. Sample bags for SPIM-FCS: [A] Sample bag made from Lumox Folie 25M, [B] mounted sample bag in the microcope SPIM-2 (without sample chamber).

S1.4. Confocal FCS measurements 1

The confocal FCS setup used in Singapore was described previously [6] and we will provide only a brief description of the instrument. The confocal FCS system is based on a modified Olympus FV 300 confocal microscope (Olympus, Tokyo, Japan). Fluorescence was excited with the 488 nm line of an argon ion laser (Melles Griot, Albuquerque, NM, USA), which was focused by a water-immersion objective (60x, NA 1.2; Olympus, Tokyo, Japan) into the sample. The fluorescence light emitted from the sample was collected by the same objective, was filtered by a band-pass filter (510AF23, Omega Optical, VT, USA), passed a 3x magnification system and was spatially filtered by a 150 μm pinhole. The light from the pinhole was imaged onto

an avalanche photodiode which operated in photon counting mode (SPCM-AQR-14-FC; Pacer, Berkshire, UK). The autocorrelation curves were computed online by a hardware correlator (Flex02-01D; Correlator.com, Bridgewater, NJ, USA). The laser power was set to 0.2 μW, as measured in front of the microscope objective. The system was calibrated with Atto488 which has a known diffusion coefficient of $D_{20,W} = (370 \pm 9)\ \mu\text{m}^2$ @ 20°C [7]. The same laser power and settings were used for the measurement of polystyrene beads and the calibration.

S1.5. Confocal FCS measurements 2

Confocal FCS measurements for comparison to the SPAD array measurements were also performed on a custom FCS setup [8], based on an inverted Olympus IX-70 microscope (Olympus, Hamburg, Germany) and a 60x/NA1.2 objective. Light from an ArKr-Laser (CVI Melles Griot, Bensheim, Germany), filtered by an AOTF (AOTF Nc, AA Opto Electronic, France) was reflected into the microscope resulting in about 3μW of laser power above the objective. Fluorescence was detected with a SPAD (SPCM-AQR-13, Perkin-Elmer, Wellesley, USA) and correlated by a hardware correlator card (ALV-5000/E, ALV Laser GmbH, Langen, Germany). Data evaluation was performed using QuickFit 3.0 [5].

S2. Determination of PSFs from bead scans

S2.1. z-scans of beads

Simple *z*-scans were done with 100 nm fluorescent microspheres (FluoSpheres YG, Invitrogen) embedded in a 0.5% PhytaGel rod (P8169, Sigma-Aldrich Chemie GmbH, Munich, Germany, supplemented with 0.1% $MgSO_4$) by scanning and recording 1000 frames in 200 nm steps. The beads were then localized automatically using a custom Matlab-script (run in Matlab 2012a, MathWorks, Ismaning, Germany). The image was segmented according to intensity and from every connected set of pixels only the one pixel with the highest intensity was used as first estimate for the bead position. The script also took care to keep a minimum distance of 3 pixels (in *x*-, *y*- and *z*-direction) between any two initial bead positions. Finally, three 1D Gaussians (cuts through the brightest pixel of each bead, along the *x*-, *y*- and *z*-axis), as well as a 3D Gaussian function were fitted to each bead (for examplary results see Fig. S8 and Fig. S12(b)). The 3D Gaussians were allowed to be tilted a bit, to account for a slight misalignment of the xyz-stage (see especially Fig. S8(B)). Unreasonably small or large results were excluded from the dataset before calculating averages.

From the method described in the last paragraph, the $1/e^2$-width $\psi_{xy}(w_{xy})$ from 3D fits was extracted. Then the contribution of the finite pixel size has to be corrected for: For this correction a 1D molecular detection efficiency (MDE) function was set up:

$$\text{MDE}(x; a, w_{xy}) = \text{Rect}(x; a) \star \text{PSF}(x; w_{xy}) = \frac{1}{\mathcal{N}} \int_{-a/2}^{a/2} \exp\left(-2 \cdot \frac{(x - \xi)^2}{w_{xy}^2}\right) d\xi \qquad (1)$$

where $\text{Rect}(x; a)$ is 1 for $-a/2 \leq x \leq a/2$ and 0 anywhere else (i.e. *a* is the pixel width), w_{xy} is the $1/e^2$-width of the Gaussian PSF $\text{PSF}(x; w_{xy})$, $\star$ denotes a convolution and $\mathcal{N}$ is a normalization constant. Then a simple 1D-Gaussian $\text{PSF}(x; \psi_{xy})$ was fitted to Eq. (1), using a least-squares scheme. From the resulting plot $\psi_{xy}(w_{xy})$ (see Fig. S7) the corrected w_{xy} can be read.
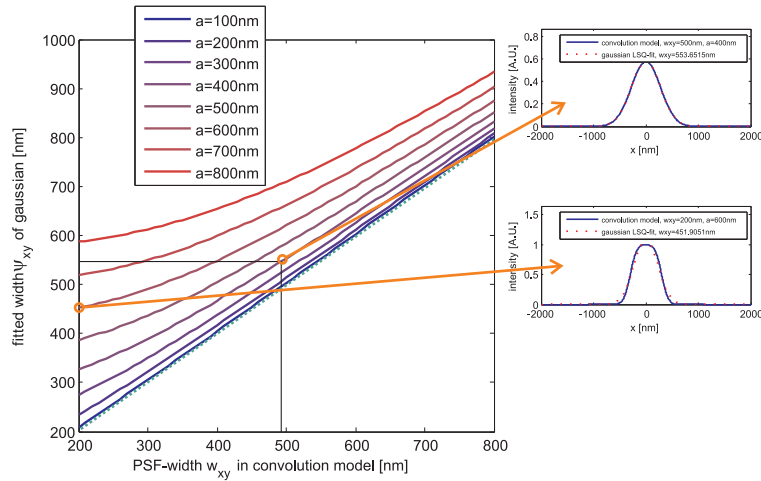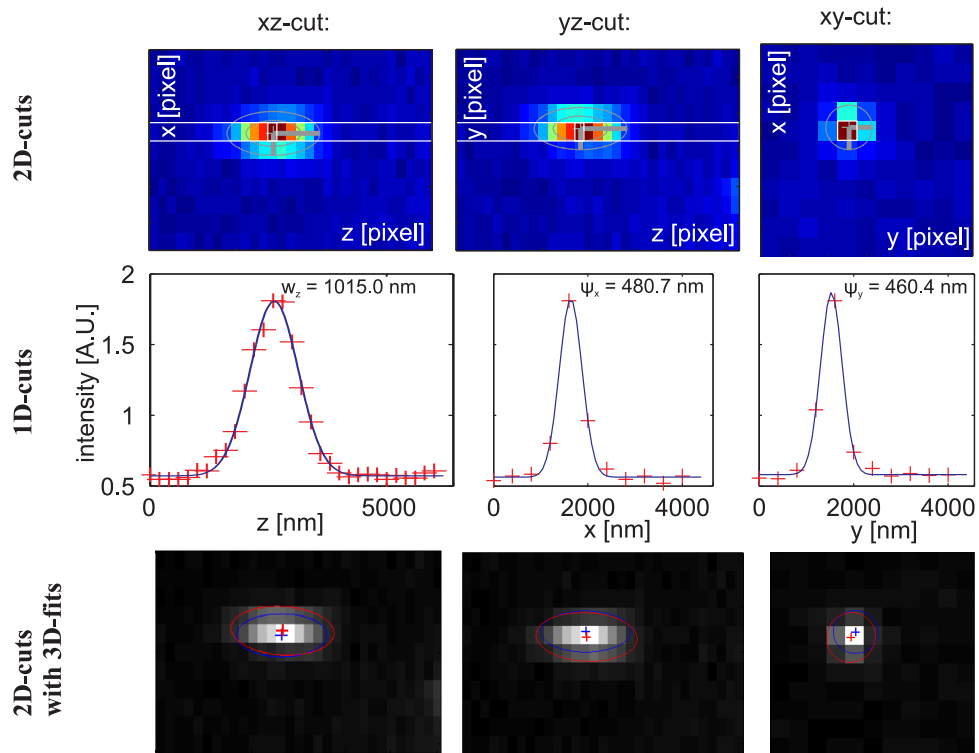

Fig. S7. Plot of the width of a Gaussian function fitted to the pixel MDE in Eq. (1) for different pixel-widths *a*. The curve $\psi_{xy}(w_{xy}) = w_{xy}$ is shown in green. On the RHS two example MDE curves (blue) and fits (red, dotted) are shown.

[A]: Bead scans of Andor iXon X3 860 with a 60x/NA1 objective
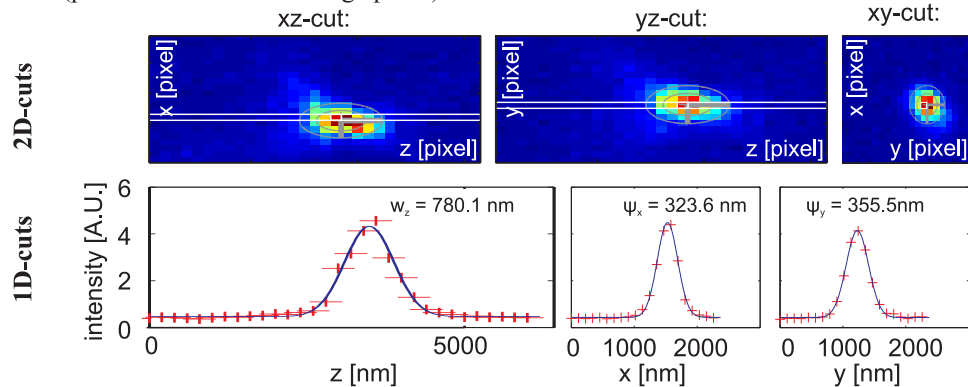(pixel size ~400nm in image plane)

Fig. S8. Example PSFs as determined with bead scans for [A] an Andor *iXon X3 860* EMCCD camera (*x-/y*-pixel size 400 nm, *z*-pixel size 200 nm) and [B] and *pco.edge* sCMOS camera (*x-/y*-pixel size 108 nm, *z*-pixel size 200 nm). In the top row three 2D cuts through the brightest pixel of the bead are shown. The three plots below show 1D-fits (blue line) of a Gaussian function to 1D cuts (red points) along the *x*-, *y*- and *z*-axis through the brightest pixel. In [A] also the results of 3D-Gaussian fits (red in third row) are compared to the 1D-fits (blue in third row).

S2.2. Results for different cameras

For the *iXon X3 860* EMCCD (pixel size 24 μm and thus 400 nm in the image plane) we got a $1/e^2$-width of the 3D Gaussian fit of $\psi_{xy} = (540 \pm 70)$ nm. Taking the broadening due to the rectangular pixel into account, this results in a $1/e^2$-width of the PSF of $w_{xy} \approx 490$ nm. The longitudinal $1/e^2$-width in the 3D Gaussian fits was $w_z = (1160 \pm 140)$ nm. So the MDE has an approximated axial ratio around 2.4.

For the *pco.edge* sCMOS with its small pixels (6.5 μm pixel size, i.e. 108.3 nm in the image plane), a significant correction due to pixel-size is only necessary for higher binning. Here we determined the PSF for different binnings between 1 (108×108 nm^2) and 8×8 (866×866 nm^2). The results are shown in Fig. S9. In subplot Fig. S9(A) the effect of the pixel size on the longitudinal size w_z of the MDE can be seen ("pinhole" effect).
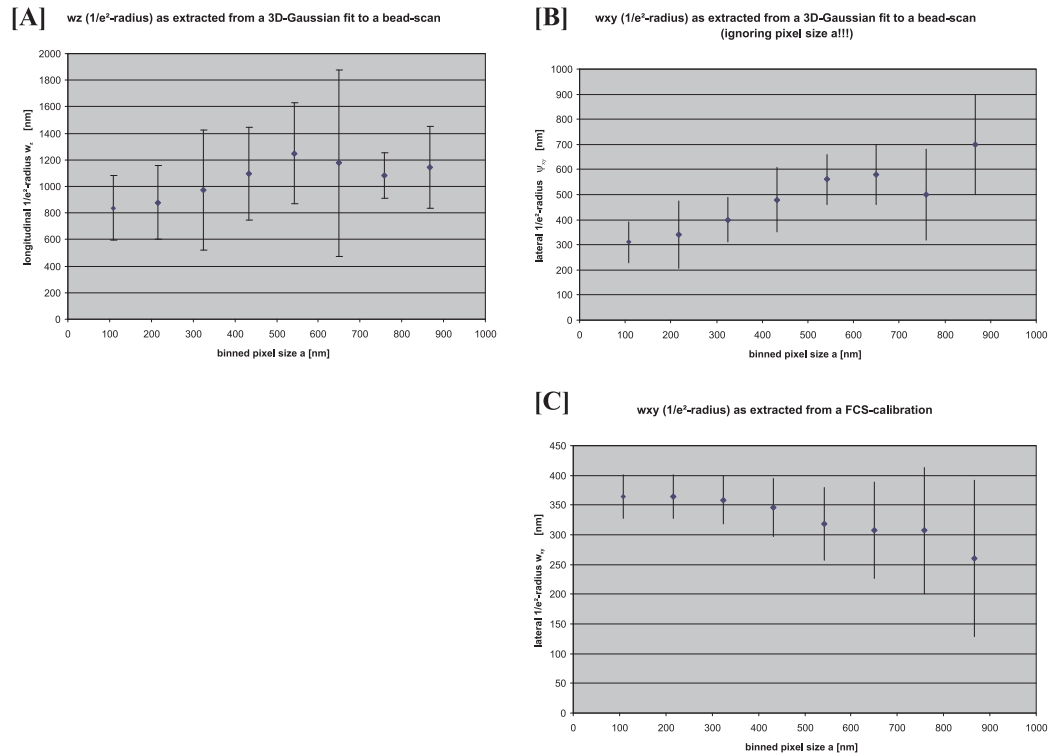

Fig. S9. PSF determination as a function of the (binned) pixel size *a* for the *pco.edge* sCMOS camera. [A] longitudinal width w_z of the MDE, extracted from a 3d Gaussian fit to a bead *z*-scan. [B] lateral width ψ_{xy} extracted from the same fit and [C] PSF-width w_{xy} extracted from a FCS-calibration, as described in the article and section S3.

S2.3.   Deviations from the ideal Gaussian focus shape

As mentioned in the main text the shape of the PSF is assumed to be Gaussian in z-direction and should follow Eq. (1) in x- and y-direction with a w_{xy} independent of x, y and z. To check this condition, we performed 1D Gaussian fits to cuts at different z-positions through each bead. Some example results are shown in Fig. S10(a-b). We fitted the resulting data $w_{xy}(z)$ to the function

$$w(z) = w_0 \cdot \sqrt{1 + \left(\frac{z}{z_0}\right)^2},$$

(2)

which describes the increasing width of the lateral intensity distribution in a Gaussian beam with beam waist w_0 and depth of focus z_0 [12]. Also in most of the bead images low-intensity sidelobes (rings near the end of the bead) are visible, as shown in Fig. S10(b-c).

To estimate the impact of these properties of the real MDE on FCS measurements with a simpler model, we performed simulations that are described in section S5. A short discussion of these effects (especially with respect to the concentration determination) can also be found in the main text.
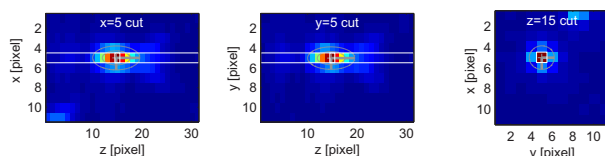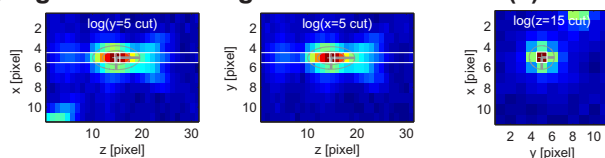
(a) *x*-cut fit results:
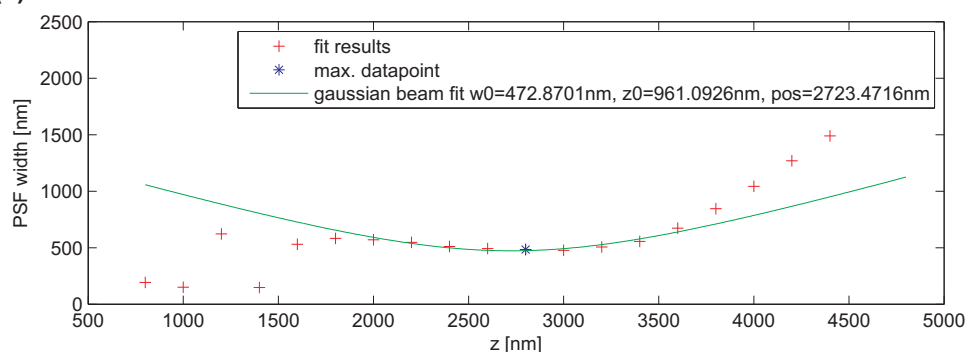
(b) *y*-cut fit results:
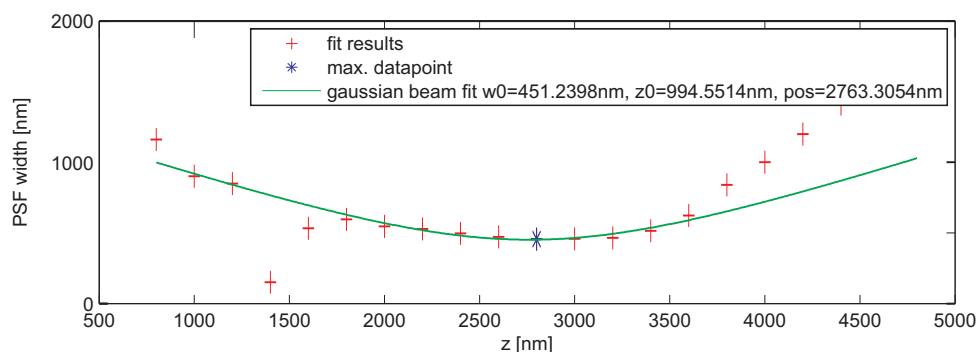
(c) images of the bead from (a) and (b)

(e) fit to z-cut for the shown bead

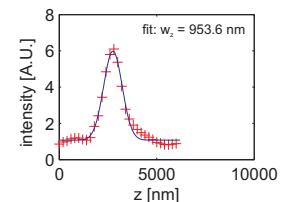**(d) logarithmized images of the bead from (a) and (b)**

Fig. S10. Example fits to a single bead from a *z*-beadscan on the *iXon X3 860* on SPIM-2: (a) and (b) show the results of Gaussian fits to several *x*- and *y*-cuts through the bead at different *z*-positions. The green line is a fit of Eq. (**??**) to this dataset. (c) and (d) show images of the scanned bead, where the sidelobes are clearly visible and (e) shows a Gaussian fit through a *z*-cut of the bead for comparison.

S2.4. *Results for the Radhard2 SPAD array*

The PSF of the *Radhard2* sensor was determined with three different methods: First, simple *z*-scans as described above (results, see Tab. ST1) were performed. Due to the large SPAD separation of 1 μm, the lateral PSF-width could not be determined reliably with this method. So as a second method, a combined *xz*-or *yz*-scan was performed, moving the same gel rod as above 20 steps (200 nm each) in *x*- or *y*-direction (i.e. 4 SPAD-pixels) and then 500 nm in *z*-direction (see Fig. S11(c)). This was repeated 100 times. From the resulting image-stack a

Matlab script extracted *xz*-cuts through beads, by recording the intensity for each row from one pixel which was shifted by 4 pixels on each *z*-movement. The initial bead positions were selected manually from the image stack. A 2D Gaussian function was fitted to each of these 2D cuts (for an example, see Fig. S11(d)). Unreasonably small or large results were excluded from the calculated averages (lateral half width $> 1\,\mu$m, longitudinal width $> 1\,\mu$m, axial ratio $1 < K < 5$). The exclusion parameters were adjusted for each dataset separately, judging by a first and unconstrained run.

Finally the diffusion coefficient D and the lateral focal $1/e^2$-radius w_{xy} were extracted from fits of dual-focus cross-correlation measurements with 100 nm beads. Raw data was acquired using the SPAD array and crosscorrelations between two pixels, which were 1 pixel apart (i.e. $1\,\mu$m) were calculated in software using the multi-scheme with one monitor per correlation channel implemented in QuickFit 3.0 [5] and described in detail in [4]. The resulting ACFs were fitted to the standard model function for 2-focus crosscorrelation (2fFCCS) of two Gaussian
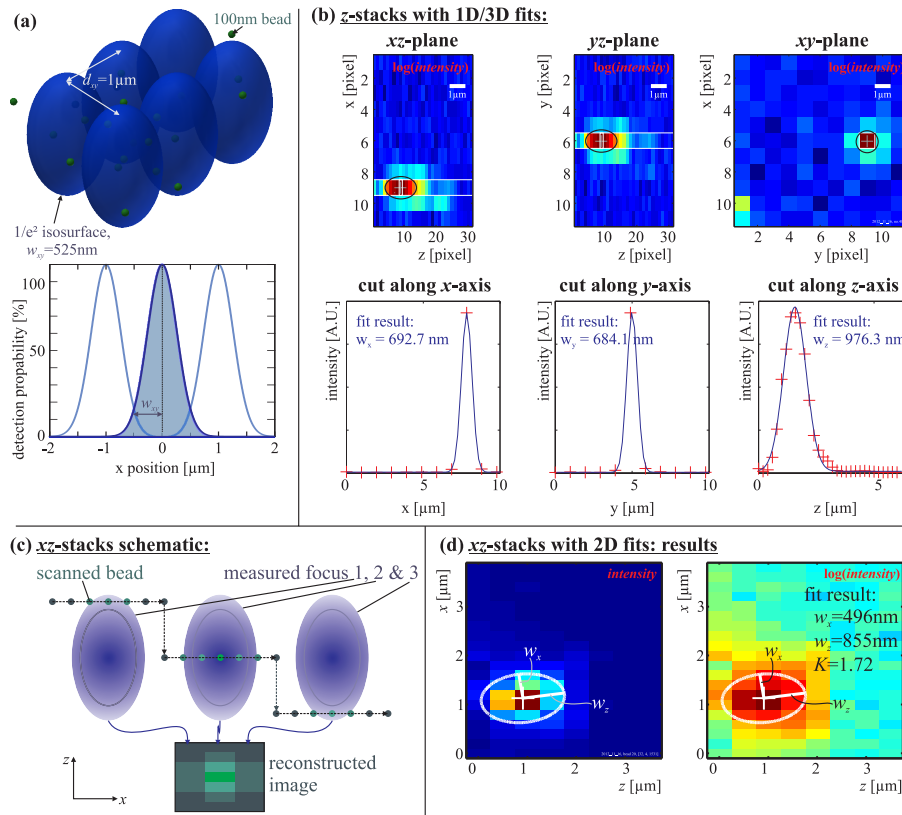
Fig. S11. Determination of *Radhard2*-PSF: (a) schematic view of the distribution of the SPAD array focal volumes in the sample (shown are the $1/e^2$-isosurfaces of Gaussian volumes) and of a cut through the detection probability inside the focal plane (b) example data from a z-bead scanning experiments on the SPAD array with 1D-fits (graphs below the images) and 2D-fits (black ellipses inside the images, showing $1/e^2$ iso lines) (c) schematic sketch of the xz-stack experiments, where a 100 nm bead is scanned in two directions and (d) results from the experiments depicted in (c) with 2D fit results as white ellipses ($1/e^2$ iso lines). The parameters $w_{xy} = 525$ nm and $K = 1.71$ were chosen for all schematic foci in this Fig.

foci [13]:

$$g(\tau) = G_\infty + \frac{1}{N} \cdot \left(1 + \frac{4D \cdot \tau}{w_{xy}^2}\right)^{-1} \cdot \left(1 + \frac{4D \cdot \tau}{K^2 \cdot w_{xy}^2}\right)^{-1/2} \cdot exp\left[-\frac{d_{xy}^2}{w_{xy}^2 + 4D \cdot \tau}\right] \qquad (3)$$

Here G_∞ is an offset value, N is the number of particles in the focus and d_{xy} is the separation between the two foci. The axial ratio of the foci was fixed to $K = (1.71 \pm 0.13)$ as obtained from the average of the determinations above. This fit is most sensitive to the diffusion coefficient and the distance between the foci, not their individual size, so the resulting D can be trusted, but not the w_{xy}. In a final step the values $D = (4.84 \pm 0.53)\ \mu m^2/s$ and $K = (1.71 \pm 0.13)$ were fixed for a fit to the autocorrelation curves (model as above Eq. (3), but with $d_{xy} = 0$) to determine w_{xy}. All results are summarized in Tab. ST1 and example curves can be seen in Fig. S12.

All models were fitted using a Levenberg-Marquardt scheme to an average over the central 16×8 correlations curves (limiting the observation to a region where the light sheet thickness changes only marginally) acquired on the *Radhard2* with 3 μs minimal lag time. The per-lag standard deviation from this average was used to weight the fit. From these 128 curves outliers (e.g. caused by aggregates or broken pixels) were removed before averaging. Usually between 1 (only one broken pixel in this range) and 30 (many aggregates) curves had to be discarded. The selection was done using an automatic scheme, which excludes all pixels below the 5% and above the 95% quantiles of the correlation amplitude distribution for low lag times. To exclude the small amount of SPAD afterpulsing observed during the measurements, the first few (<3) correlation channels were cut from the dataset before fitting.

The diffusion coefficient from the 2f-FCCS fit corresponds nicely to the expected value for 100 nm spheres ($D_{20} = 4.29\ \mu m^2/s$, from $D = k_B T/(6\pi\eta R_h)$ with Boltzmans constant k_B, absolute temperature T, viscosity η and hydrodynamic radius R_h). The lateral focal half-width acquired using this value from a single-focus-FCS measurement fits the values obtained from bead scans. Here the *xz*-scan with 2D-fit seems to be most reliable, as it resolves the PSF best. In the simple *z*-stacks, the PSF is only between 2 and 4 pixels wide, so an estimate of the three parameters of a Gaussian function (amplitude, width and position) is inaccurate (see Fig. S11(b)), especially considering the image noise. The axial ratio does not seem to depend too much on the type of fit. All PSF determination methods show that the assumption of a Gaussian PSF is sound for our SPAD array. Fig. S5 also shows a schematic of how the focal volumes distribute in the sample.

Table ST1. Results for the determination of the SPAD array PSF with different methods. All values are given as (mean ± S.D.) either over the given number of beads or over several fits at different sample concentrations between 0.1 nM **and** 1.3 nM **and at different laser powers. The temperature was 24.5-25°C during all measurements.**

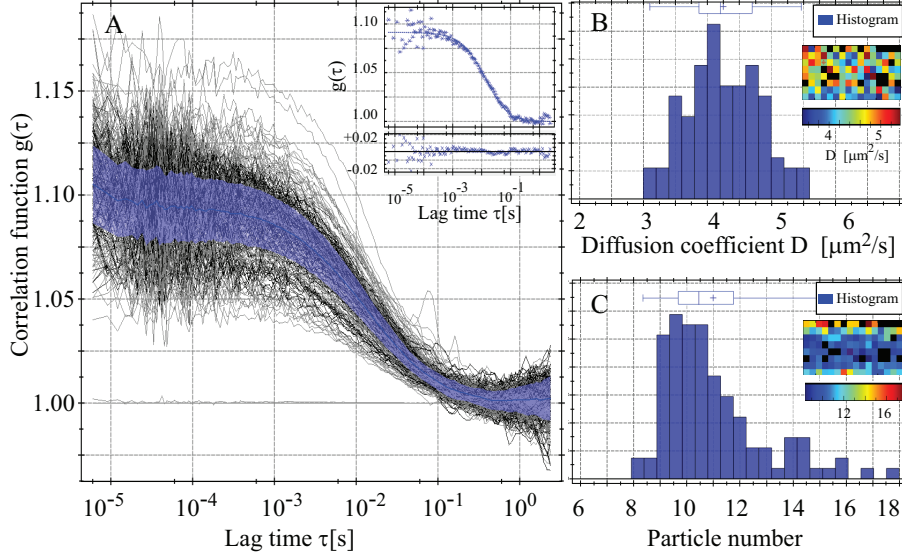|	*xy*-scans, 2D	*z*-stack 1D	*z*-stacks, 3D	2f-FCCS $d_{xy} = 1\ \mu$m, $K = 1.71$	FCS $D = 4.84\ \mu m^2/s$, $K = 1.71$
Beads	89	84	70	—	—
w_{xy} [nm]	580±180	642±221	637±192	8743±41	523±59
w_z [nm]	1080±300	887±198	950±225	1271±70	857±95
$K = w_z/w_{xy}$	1.83±0.46	1.57±0.64	1.73±0.73	1.71, fix	1.71. fix
$D_{25}\ [\mu m^2/s]$	-	-	-	4.84±0.53	4.84, fix
$D_{20}\ [\mu m^2/s]$	-	-	-	4.23±0.46	4.23, fix

Fig. S12. Example fit data from *Radhard2* SPAD array. [A] shows all autocorrelation curves from one measurement (all pixels). Grey curves are masked (criterion, see text) and the blue curve is the average and standard deviation over all unmasked ACFs. The inset displays a random pixel's data together with a fit (dashed line) and the residuals below. [B] and [C] show parameter images (pixel-size 1 μm) and histograms of the diffusion coefficient and particle number acquired in a 1-component fit. The measurement was performed for a solution with $c_{set} = 0.76$ nM at 25°C and 60.4 W/cm² laser intensity.

S3. PSF calibration using SPIM-FCS

We give a brief descrption of the PSF calibration performed for the different cameras using SPIM-FCS here. The principle method was described in detail in Ref. [10]. Here is a short summary:

1. For calibration SPIM-FCS was measured on a diluted solution of 100 nm fluorescent microspheres in a sample bag.

2. The longitudinal width w_z of the MDE was either estimated from the light sheet width (for large pixels) or from a bead scan (especially for small pixels, cf. section S2.2).

3. Autocorrelation functions were calculated using ImFCS or QuickFit 3.0 for different binnings of the pixels. Usually a binning between 1×1 and 5×5 was used for the 24 μm pixels of the Andor *iXon X3 860*. Depending on the number of pixels in the central 8×8 μm², larger binnings may be needed (e. g. for the sCMOS cameras with 6.5 μm pixels).

4. At large pixel sizes $a \gg w_{xy}$ (higher binnings), the diffusion coefficient measured with SPIM-FCS is mostly independent of the value of w_{xy} (see Fig. S13). The different sets of ACFs were fitted with the standard SPIM-FCS model (see main article, eq. (1)). the parameters a and w_z were fixed to their known values (from the respective binning and step 2). The fits were performed for different values of w_{xy} choosen around the expected value of w_{xy} (e.g. between 400 nm and 800 nm). For increasing binning the curves w_{xy} against the pixel size a converge against the true diffusion coefficient D. Finally the value of D is calculated by averaging the fit results of all different w_{xy} at the largest binnings.

5. Finally the unbinned data was fitted again, now using the diffusion coefficient D determined in the last step and a and w_z still fixed. From this final fit a good estimate of the lateral focal size w_{xy} can be extracted.
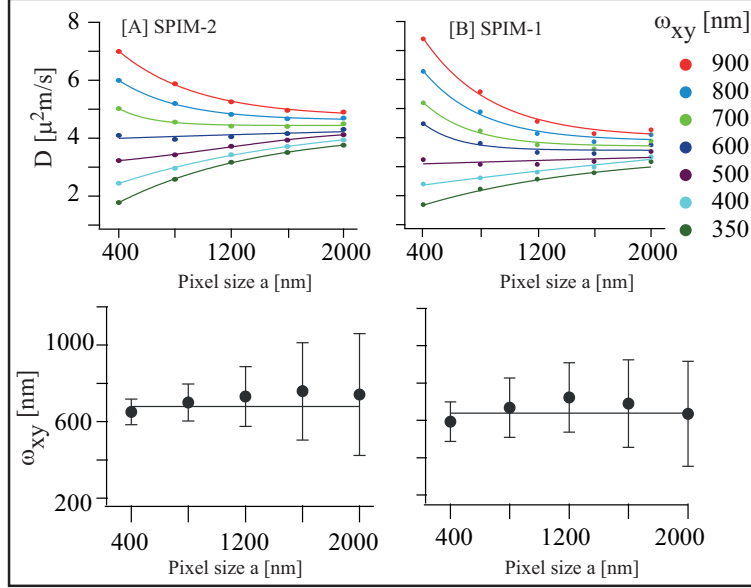

Fig. S13. Example fit data from a SPIM-FCS calibration for a *iXon X3 860* mounted on two different SPIM microscopes : [A] SPIM-2 (DKFZ, Germany) and [B] SPIM-1 (NUS, Singapore). The upper graphs show fit results at different binnings and for different fixed w_{xy}(as described in step 4, exponential fits as lines to guide the eye). The lower graphs are fit results for $w_{xy}$from step 5 (average and standard deviation from all pixels) with the diffusion coefficient from step 4 fixed. The black line is the average over all binnings.

S4. Camera Noise

We also characterized the camera noise, by comparing the signal and background intensity statistics. For both, we calculated averages and standard deviations. As both properties depend on the instrument characteristics (light sheet intensity, signal attenuation in the detection beam path ...) and the sample, we decided to collect the results separately for the two instruments SPIM-1 and SPIM-2. All data for one instrument should be comparable. A matching between the instruments can be done by comparing the data for the Andor *iXon X3 860*, which was measured on both. Tab. ST2 summarizes the results. For each camera we performed a measurement of a $\sim$ 1 nM solution of 100 nm fluorescent microspheres. Then for each pixel's time series $I_{xy}(t)$, the average intensity $I_{xy} = \langle I_{xy}(t) \rangle_t$ and its standard deviation $\sigma_{I_{xy}}$ were calculated. Tab. ST2 gives the average

$$\langle I \rangle = \frac{1}{X \cdot Y} \cdot \sum_{x=1}^{X} \sum_{y=1}^{Y} I_{xy} \tag{4}$$

and (after ±) the standard deviation

$$\sigma_I = \sqrt{\frac{1}{X \cdot Y - 1} \cdot \sum_{x=1}^{X} \sum_{y=1}^{Y} (I_{xy} - \langle I \rangle)^2} \tag{5}$$

over all the pixels in each measurement, so the latter characterize the variation inside a single frame. The table also contains data acquired without illumination ("background").

Table ST2. Camera noise characterization obtained for [A] SPIM-1 and [B] SPIM-2. Signal intensities and their standard deviation (S.D.) are either given as photons/second or in grey levels (depending on the type of detector), but always in the same units in a single column. The given numbers are the statistics as explained in the text and equations Eq. (4) and Eq. (5). The numbers in parentheses are the relative standard deviations. All measurements on one SPIM were performed for the same sample and (otherwise noted differently) at the same laser intensities.

[A] SPIM-1:

	iXon X3 860[†]	ORCA-Flash4.0
exposure time [μs]	450	623
cycle time [μs]	495	625
signal, mean $\langle I - I_B \rangle$	1558 ± 20 (1.3%)	8.2 ± 1.8 (22%)
signal, S.D. σ_{I-I_B}	97 ± 3 (3%)	7.2 ± 0.8 (11%)
background, mean $\langle I_B \rangle$	100 ± 2 (2%)	101.3 ± 0.7 (0.7%)
background, S.D. σ_{I_B}	3.12 ± 0.03 (1%)	2.7 ± 1.1 (41%)
$\sigma_{I_B}/\sigma_{I-I_B}$	3.2%	38%
$\sigma_{I_B}/\langle I - I_B \rangle$	0.2%	33%

[†] EM-gain for the Andor *iXon X3 860* EMCCD camera on SPIM-1 was 50

[B] SPIM-2:

	iXon X3 860[†]	pco.edge	Radhard2
exposure time [μs]	450	486	501
cycle time [μs]	489	495	501
signal, mean $\langle I - I_B \rangle$	1806 ± 35 (2%)	42.3 ± 4.9 (12%)	11855 ± 792 (7%)
signal, S.D. σ_{I-I_B}	453 ± 28 (6%)	25.6 ± 2.2 (9%)	5486 ± 12 (0.2%)
background, mean $\langle I_B \rangle$	97.8 ± 5.4 (6%)	378 ± 12 (3%)	150 ± 55 (37%)
background, S.D. σ_{I_B}	3.75 ± 0.07 (2%)	4.8 ± 1.9 (40%)	546 ± 71 (13%)
$\sigma_{I_B}/\sigma_{I-I_B}$	0.8%	18.8%	10%
$\sigma_{I_B}/\langle I - I_B \rangle$	0.2%	39.0%	4.6%

[†] EM-gain for the Andor *iXon X3 860* EMCCD camera on SPIM-2 was 50

S5. FCS simulations

In order to quantify the impact of a more realistic PSF model (compare also section S2.3) on the measurement results, we performed FCS simulations. We used the same (but extended) simulation program already used in [4] and [11]. Basically from a set of 3D random walk trajectories

$$\vec{r}_i(t), t = 0...T_{\mathrm{sim}}, i = 1..K, \tag{6}$$

the estimated average number of detected photons for each timestep $[t, t + \Delta t_{\mathrm{sim}}]$ is calculated:

$$\overline{N}_{\mathrm{phot}}(t) = \overline{N}_0 \cdot \Delta t_{\mathrm{sim}} \cdot \sum_{i=1}^{K} q_{\mathrm{f}} \cdot q_{\mathrm{det}} \cdot \underbrace{I_{\mathrm{ill}}(\vec{r}_i(t)) \cdot \mathrm{CEF}(\vec{r}_i(t))}_{=:\mathrm{MDE}(\vec{r})}. \tag{7}$$

Here $\overline{N}_0$ is the maximum number of detected photons per fluorophore and time step, while q_f and q_{det} are the quantum efficiencies of fluorescence and detection. As in the main article, the illumination distribution is denoted by $I_{ill}(\vec{r})$ and the collection efficiency function by $CEF(\vec{r})$. Then the detected number of photons $N_{phot}(t)$ is calculated by drawing a random number from a Poissonian distribution with average $\overline{N}_{phot}(t)$. Other detector statistics are possible here. Finally the measured fluorescence intensity timetrace $N_{phot}(t)$ is correlated with a multi-τ scheme to yield the simulated autocorrelation function.

We tested several possible combinations for the illumination and detection:

1. **Gaussian**: Both are assumed to be Gaussian with final widths of their product $MDE(\vec{r})$ of $w_{xy} = 500$ nm and $w_z = 1200$ nm:

$$MDE(x,y,z) = \exp\left(-2 \cdot \frac{x^2 + y^2}{w_{xy}^2} - 2 \cdot \frac{z^2}{w_z^2}\right) \tag{8}$$

2. **Gaussian beam**: The illumination is Gaussian and the detection has the form of a Gaussian beam:

$$CEF(x,y,z) = \left(\frac{w_0}{w(z)}\right)^2 \cdot \exp\left(-2 \cdot \frac{x^2 + y^2}{w^2(z)}\right), \quad \text{with} \quad w(z) = w_0 \cdot \sqrt{1 + \left(\frac{z}{z_0}\right)^2} \tag{9}$$

The parameters w_0 and z_0 were chosen, so a Gaussian fit to $MDE(x,0,0)$ and $MDE(0,0,z)$ yielded $w_{xy} = 500$ nm and $w_z = 1200$ nm respectively.

3. **Gaussian beam & slit**: The detection is again a Gaussian beam as in 2 and the illumination is a slit function:

$$I_{ill}(x,y,z) = \left(\frac{\sin(\pi \cdot z/z_0)}{\pi \cdot z/z_0}\right)^2 \tag{10}$$

Again the parameter z_0 was choose so a fit to $MDE(x,0,0)$ and $MDE(0,0,z)$ yielded $w_{xy} = 500$ nm and $w_z = 1200$ nm respectively.

The simulations were performed for a random walk with diffusion coefficient $D_{real} = 50\,\mu m^2/s$ and the resulting correlation curves were all fitted with a simple 3D Gaussian model with $w_{xy} = 500$ nm and $w_z = 1200$ nm:

$$g(\tau) = \frac{1}{N} \cdot \left(1 + \frac{4D \cdot \tau}{w_{xy}^2}\right)^{-1} \cdot \left(1 + \frac{4D \cdot \tau}{w_z^2}\right)^{-1/2} \quad \text{with} \quad c := \frac{N}{\pi^{3/2} w_{xy}^2 w_z} \tag{11}$$

The fit results are summarized in Tab. ST3, which shows clearly that the diffusion coefficient can be acquired accurately and the concentration is overestimated due to the underestimated focal volume by the assumtion of a false fit model. Including sidelobes even makes this situation worse. Fig. S14 shows representative images of the different focis' $MDE(x,y,z)$.

| concentration	focus	$D[\,\mu\mathrm{m}^2/\mathrm{s}]$	$(D - D_{\mathrm{real}})/D_{\mathrm{real}}$	$c[nM]$	$(c - c_{\mathrm{real}})/D_{\mathrm{real}}$
$c_{\mathrm{real}} = 0.1$ nM	Gaussian	53.6	7.2%	0.105	5%
	Gaussian beam	47.5	-5.0%	0.136	36%
	Gaussian beam& slit	48.0	-4.0%	0.141	41%
$c_{\mathrm{real}} = 0.2$ nM	Gaussian	52.6	5.2%	0.223	12%
	Gaussian beam	47.1	-5.8%	0.286	43%
	Gaussian beam& slit	48.2	-3.6%	0.295	48%
$c_{\mathrm{real}} = 0.5$ nM	Gaussian	56.4	12.8%	0.506	1%
	Gaussian beam	51.5	3.0%	0.657	31%
	Gaussian beam& slit	52.1	4.2%	0.688	38%
$c_{\mathrm{real}} = 1.0$ nM	Gaussian	48.2	3.6%	1.074	8%
	Gaussian beam	47.0	-6.0%	1.339	34%
	Gaussian beam& slit	47.1	-5.8%	1.412	41%

Table ST3. Fit results for FCS simulations
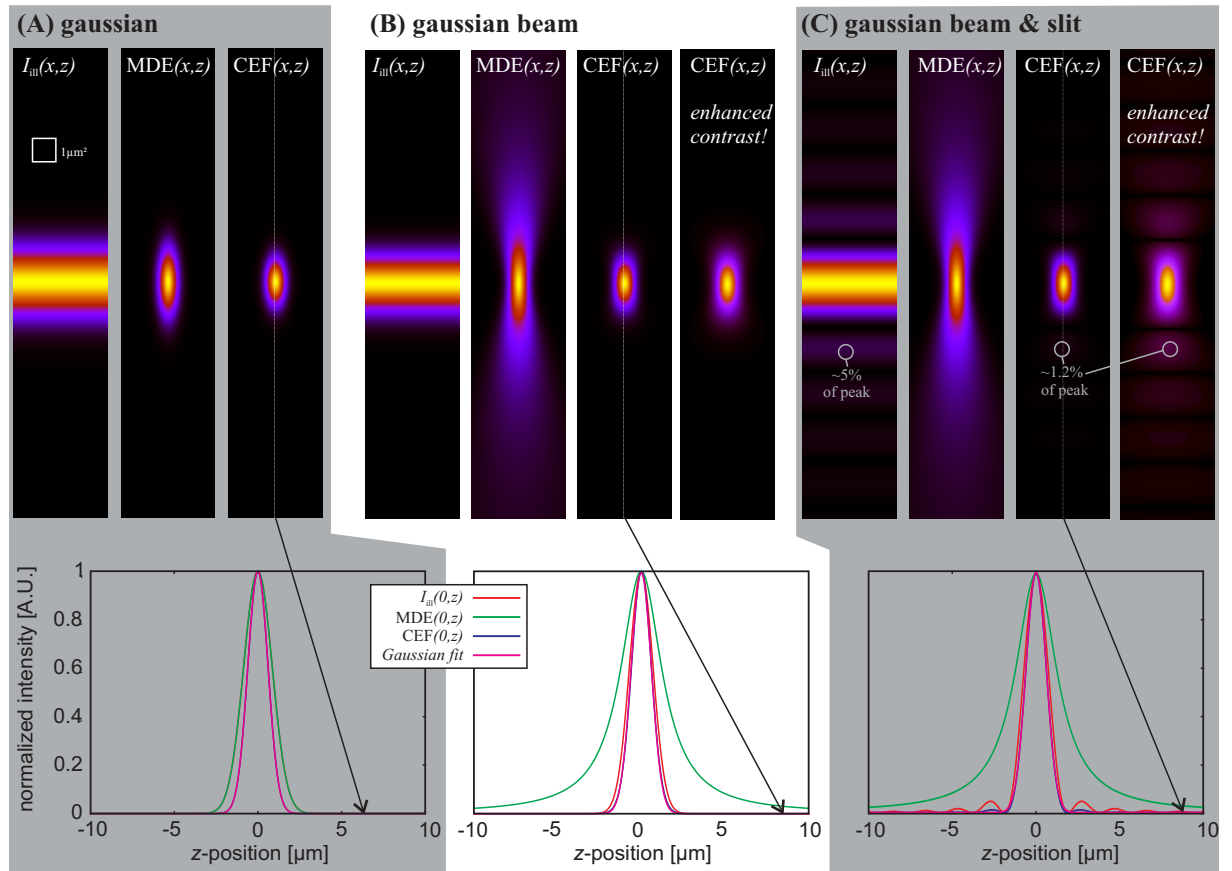
Fig. S14. Focus shapes for the FCS simulation. Top row: xz-cut through the FCS simulation foci. Bottom row: cuts (and Gaussian fits) along the z-axis, as indicated in the CEF-images in the top row.